

Semi-Analytical Expression of G-Mode Period Spacing:  
The Case of Brunt-Väisälä Frequency with Not a Jump But a Ramp

YOSHIKI HATTA<sup>1,2,3</sup>

<sup>1</sup>*Department of Astronomical Science, School of Physical Sciences, SOKENDAI  
2-21-1 Osawa, Mitaka, Tokyo 181-8588, Japan*

<sup>2</sup>*National Astronomical Observatory of Japan  
2-21-1 Osawa, Mitaka, Tokyo 181-8588, Japan*

<sup>3</sup>*Institute for Space-Earth Environmental Research, Nagoya University  
Furo-cho, Chikusa-ku, Nagoya, Aichi 464-8601, Japan*

ABSTRACT

To decipher complex patterns of gravity-mode period spacings observed for intermediate-mass main-sequence stars is an important step toward the better understanding of the structure and dynamics in the deep radiative region of the stars. In this study, we apply JWKB approximation to derive a semi-analytical expression of the g-mode period spacing pattern, for which the gradient in the Brunt-Väisälä frequency is taken into account. The formulation includes a term  $P^{-1}B_{\star}$ , where  $P$  and  $B_{\star}$  represent the g-mode period and degree of the structural variation, the latter of which especially is related to the steepness of the gradient of the Brunt-Väisälä frequency. Tests with 1-dimensional stellar models show that the semi-analytical expression derived in this study is useful for inferring the degree of the structural variation  $B_{\star}$  with accuracy of  $\sim 10\%$  in the case of relatively massive intermediate-mass models with the mass  $M$  larger than  $3M_{\odot}$ . The newly formulated expression will possibly allow us to put further constraints on, e.g., mixing processes inside intermediate-mass main-sequence g-mode pulsators such as  $\beta$  Cep, SPB, and  $\gamma$  Dor stars that have been principal targets in asteroseismology.

*Keywords:* Asteroseismology (73) — Stellar oscillations (1617) — Stellar interiors (1606) — Stellar cores (1592) — Stellar evolution (1599)

1. INTRODUCTION

Modern space-borne missions such as Kepler (Koch et al. 2010) and TESS (Ricker et al. 2014) have enabled us to detect non-radial oscillations of tens of thousands of stars with unprecedentedly high precisions ( $\sim 10^{-5}$  mag), bringing about the firm establishment of asteroseismology (e.g. Aerts et al. 2010). Main-sequence gravity-mode pulsators (e.g.,  $\gamma$  Dor stars, SPB stars, and  $\beta$  Cep stars) are of particular importance since, based on measurements of the g modes, we can probe the deep radiative region of these stars (e.g. Unno et al. 1989), thus far leading to numerous significant constraints on theories of, for instance, the angular momentum transfer or the chemical element transport deep inside stars (e.g. Aerts et al. 2019)

One remarkable feature often seen in observed spectra of g-mode pulsators is that g-mode peaks are almost equidistantly spaced in periods (e.g. Degroote et al. 2010a; Papics et al. 2014, 2015; Van Reeth et al. 2015). This observational characteristic can be explained by the asymptotic theory of stellar non-radial oscillation (e.g. Tassoul 1980) where local wavelengths of the waves are assumed to be much shorter than the scale height of the background (c.f. geometrical optics). In such a high-order limit, the g-mode period spacing, which is defined as the difference between two g-mode periods with the neighboring radial order  $n$  and the same spherical degree  $l$ , is constant:

$$\Delta P_g = \frac{2\pi^2}{\sqrt{l(l+1)}} \left[ \int_{r_0}^{r_1} \frac{N}{r} dr \right]^{-1}, \quad (1)$$

where  $N$  and  $r$  represent the Brunt-Väisälä (BV hereafter) frequency and the distance from the center. The bottom and top of the g-mode cavity are denoted by  $r_0$  and  $r_1$ , respectively. Since the integration in the right-

hand side of Equation (1) increases almost monotonically along with stellar evolution (Miglio et al. 2008), the g-mode period spacing can be used for inferring the evolutionary stage of stars (e.g. Bedding et al. 2011; Kurtz et al. 2014; Saio et al. 2015).

Although the almost constant g-mode period spacings indicate that the observed g modes are indeed high-order enough to closely follow the simple asymptotic relation (1), it is nevertheless usually the case that observed g-mode period spacings exhibit statistically significant deviation from constancy, which is often characterized by oscillatory patterns around the constant value given by Equation (1) (e.g. Degroote et al. 2010b; Van Reeth et al. 2015; Pedersen et al. 2018; Garcia et al. 2022a). These oscillatory patterns are interpreted as a representation of mode trapping (Brassard et al. 1992; Montgomery et al. 2003; Miglio et al. 2008); a sharp variation in the BV frequency must be taking place with the scale height comparable to (or smaller than) a typical local wavelength of gravity waves there, rendering some particular g modes to be “trapped” in a certain region. Such a sharp variation in the BV frequency (also called “buoyancy glitch”) is, in the case of main-sequence g-mode pulsators, considered to be related to a steep chemical composition gradient in the deep radiative region just above the convective core that is left by the receding nuclear burning core (Miglio et al. 2008).

Importantly, it has been theoretically shown that the location and degree of a sharp variation in the BV frequency determine the period and amplitude, respectively, of the oscillatory component in a g-mode period spacing pattern (e.g. Miglio et al. 2008). In other words, we can extract the information on the BV frequency profile by analyzing the observed g-mode period spacing patterns ( $\Delta P_g$  patterns hereafter). For example, various mixing prescriptions used in 1-dimensional stellar evolutionary codes can be tested by comparing the observed  $\Delta P_g$  patterns with those computed based on 1-dimensional stellar models since different mixing prescriptions lead to different BV frequency profiles, resulting in different  $\Delta P_g$  patterns. For more detail, see, e.g., Moravveji et al. (2015), Moravveji et al. (2016), Buyschaert et al. (2018), Wu and Li (2019), Wu et al. (2020), Michielsen et al. (2021), Pedersen et al. (2018); Pedersen (2022a) and references therein.

There have also been several attempts to extend the theoretical work of Miglio et al. (2008). Significant progress has been made by Cunha et al. (2019) who have explicitly derived semi-analytical expressions of the  $\Delta P_g$  pattern for main-sequence g-mode pulsators based on the asymptotic approximation and the two-zone modeling of the BV frequency to parameterize the sharp

variation in it (as will be detailed later in Section 3). As a case study, they have successfully demonstrated that the explicit expression can reproduce the  $\Delta P_g$  pattern of a main-sequence  $6 M_\odot$  model, highlighting the high potential of the semi-analytical approach to study the BV frequency profile in a rather model-independent manner.

In this study, we would like to expand upon the formulation of Cunha et al. (2019) with respect to how we model the BV frequency to derive semi-analytical expressions of the  $\Delta P_g$  pattern. As will be explained in Section 2, it becomes rather difficult to parameterize the BV frequency of less massive stars ( $\sim 1.3 - 3 M_\odot$ ) by two-zone modeling with a discontinuity because the BV frequency becomes less discontinuous as the mass of the star gets smaller; not a jump but a ramp is required to model the BV frequency. One possible alternative in the formulation of Cunha et al. (2019) is thus to take the gradient in the BV frequency into account.

It should also be instructive to remind the readers of the fact that most of the theoretical and observational studies of  $\Delta P_g$  patterns to infer the internal structures of g-mode pulsators are focusing on relatively massive ( $\sim 3 - 8 M_\odot$ ) main-sequence stars in which the BV frequency can be parameterized reasonably well by two-zone modeling with a discontinuity (e.g. Pedersen et al. 2018). In this context, our new formulation might be helpful for carrying out g-mode asteroseismology of relatively low-mass intermediate-mass stars, namely,  $\gamma$  Dor stars, for which a large number of  $\Delta P_g$  patterns have been detected so far (e.g. Van Reeth et al. 2015). (Note that the  $\Delta P_g$  patterns of  $\gamma$  Dor stars have been intensively analyzed to infer the internal rotation rate of the stars (e.g. Li et al. 2019, 2020; Saio et al. 2021; Tokuno and Takata 2022; Garcia et al. 2022b), though the oscillatory component around a constant value has not been used. We will discuss it later in Section 5.)

There are two goals in this study. One is to present a semi-analytical expression of the  $\Delta P_g$  pattern taking into account the gradient in the BV frequency. Another goal is to demonstrate how the semi-analytical expression is useful for extracting information on the BV frequency profile. We start with a brief review on internal structures of main-sequence g-mode pulsators (Section 2). Then, we present the formulation and validation of a new semi-analytical expression (Section 3). The derived expression is tested with realistic stellar models and then applied to one of the Kepler targets KIC 11145123 (Huber et al. 2014; Kurtz et al. 2014), which is a  $\delta$  Sct- $\gamma$  Dor hybrid pulsator (Section 4). It should be noted that, in the derivation of the semi-analytical expression, we neglect the effects of rotation and convective overshooting

on  $\Delta P_g$  patterns. We therefore have a few brief discussions about the impact of the negligence (Section 5). We finally conclude in Section 6.

## 2. STRUCTURE AROUND DEEP RADIATIVE REGION OF INTERMEDIATE-MASS STARS

One major goal in this section is to highlight how internal structures (especially around the deep radiative region) of main-sequence g-mode pulsators vary depending on the stellar mass and evolutionary stage. We also would like to show that the difference in internal structures leads to different behaviors of  $\Delta P_g$  patterns. To this end, we compute several evolutionary models of main-sequence stars with different masses and ages. After we explain basic setups to compute the stellar models in Section 2.1, we show internal structures of the models in Section 2.2, where a possible cause for a milder variation in the BV frequency for a lower-mass stellar model is discussed. The  $\Delta P_g$  patterns of the corresponding models are shown in Section 2.3 in order to qualitatively check the effects of the gradient in the BV frequency on the  $\Delta P_g$  pattern.

### 2.1. Models

We have used MESA (version 15140; Paxton et al. 2011, 2013, 2015, 2018, 2019) basically with its default settings to compute stellar evolutionary tracks for different masses, namely, 1.6, 3, and 6  $M_\odot$ , which roughly covers the mass range of main-sequence intermediate-mass g-mode pulsators. The same initial chemical composition  $(X, Y, Z) = (0.70, 0.28, 0.02)$  is used for the three evolutionary sequences. No magnetic field, rotation, nor convective overshooting has been taken into account.

One specific MESA option we have additionally activated in the computation is elemental diffusion (see, e.g., Paxton et al. 2018) for the purpose of eliminating apparently unphysical discontinuous features in the BV frequency around the deep radiative region. The diffusion velocities in the envelope are artificially suppressed by setting the parameter “diffusion\_v\_max” equal to  $10^{-7}$  to render the helium in the envelope not to be depleted (Morel and Thevenin 2002). Note that radiative levitation (e.g. Michaud et al. 2015) is not included.

Along with evolution, when the central hydrogen mass content  $X_c$  reaches 0.5 and 0.3, the corresponding equilibrium model is preserved whose internal structures will be shown in the next section.

### 2.2. Internal structure around the deep radiative region

As was mentioned in Section 1, the most important quantity is the BV frequency which determines g-mode periods in the high-order limit. We have thus shown

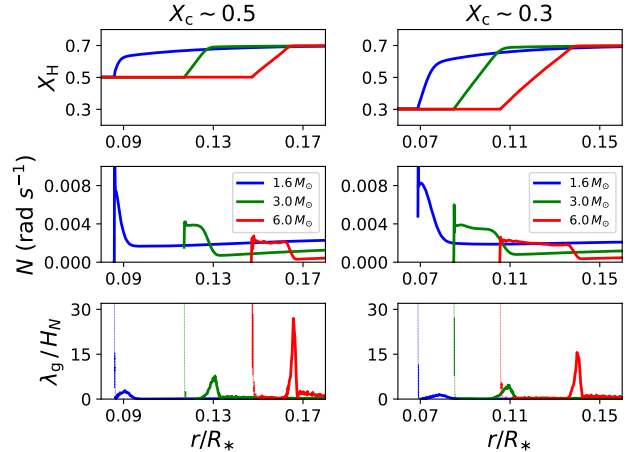


**Figure 1.** Structural parameters in the deep radiative region of stellar models with 1.6  $M_\odot$  (blue), 3  $M_\odot$  (green), and 6  $M_\odot$  (red) when the central hydrogen mass content  $X_c$  is 0.5 (left column) or 0.3 (right column). The horizontal axis is the fractional radius where  $R_*$  is the radius of the model. The hydrogen mass content  $X_H$ , the BV frequency  $N$ , and the ratio (of a typical wavelength of high-order g modes to the scale height of the BV frequency)  $\lambda_g/H_N$  are shown in this order from top to bottom. Note that  $\lambda_g/H_N$  diverges at the convective-core boundary since  $H_N \sim 0$  at the boundary. Because what we will focus on in this article is not the boundary but well inside the g-mode cavity (where  $N$  is positive), we represent the irrelevant parts of  $\lambda_g/H_N$  by thin dotted curves for visual aid.

BV frequency profiles of the six models (see middle row in Figure 1) which have been computed based on the settings described in the previous section. The corresponding hydrogen abundance profiles are presented as well (see top row in Figure 1) since the chemical composition gradient contributes to the BV frequency (see, e.g., Equation 2 in Miglio et al. 2008). All the models have the convective core where the square of the BV frequency is negative and the gravity waves are not propagative. In addition, the hydrogen abundance is uniform there. Just above the convective core lies the hydrogen abundance gradient which has been developed by the receding nuclear (and convective) core as the star evolves. Where the hydrogen abundance gradient is developed is almost identical to where the BV frequency is large, which plays an important role in mode trapping (Miglio et al. 2008).

Although all the models have similar internal structures as a whole, we notice a trend that a more massive model has a steplike BV frequency profile (see, e.g., red curves in middle panels of Figure 1) whereas a less massive model has that shaped like a slide (see, e.g., blue curves in middle panels of Figure 1). More precisely, the transition of the BV frequency ( $N$ ) between an inner re-

gion where  $N$  is large (large- $N$  region hereafter) and an outer region where  $N$  is small (small- $N$  region hereafter) is sharper for more massive models, which affects how strongly g modes are trapped in the large- $N$  region. We will explain the point in more detail in the following a few paragraphs.

Since an important point is how g modes sense the BV frequency transition, we firstly would like to quantify the degree of the BV frequency transition sensed by g modes based on the ratio of a typical local wavelength of gravity waves:

$$\lambda_g = 2\pi/k_r \sim 2\pi \frac{\omega r}{\sqrt{l(l+1)N}} \quad (2)$$

to the scale height of the BV frequency:

$$H_N \equiv \left| \frac{dr}{d \ln N} \right|. \quad (3)$$

Note that the approximation  $k_r \sim \sqrt{l(l+1)N}/\omega r$  is used where a typical angular frequency  $\omega$  is determined based on high-order g-mode frequencies of each model (more details can be found in Section 2.3), and that we only consider dipole modes ( $l = 1$ ) here. Then, where the BV frequency transition is sharp (for typical g modes) can be considered as a region with the value of the ratio  $\lambda_g/H_N$  significantly larger than unity. (In other words, the asymptotic limit of g modes corresponds to when the ratio approaches zero.)

The bottom panels of Figure 1 show the ratio  $\lambda_g/H_N$  around the deep radiative region of the stellar models. We see that the ratio  $\lambda_g/H_N$  is largest in the cases of the  $6 M_\odot$  models (red curves), meaning that the BV frequency transition of the models (sensed by g modes) is sharper than that in the other less massive models. It should be also noted that, in the  $6 M_\odot$  models, the ratio is almost zero everywhere except for in the transition region; g modes behave asymptotically in both the large- $N$  and small- $N$  regions that are separated by the sharp transition region. This is the reason why we can reasonably approximate the BV frequency of the  $6 M_\odot$  models with the two-zone modeling as was done by Cunha et al. (2019).

This is nevertheless not the case for, e.g., the  $1.6 M_\odot$  models, where the local maxima of the ratio  $\lambda_g/H_N$  are much smaller than those of the  $6 M_\odot$  models. Moreover, the width of the sharp transition region (where  $\lambda_g/H_N > 1$ ) in the  $1.6 M_\odot$  models are so broad that it overlaps almost the whole large- $N$  region; the large- $N$  and small- $N$  regions are not well separated by the transition region. Therefore, it does not seem to be appropriate to approximate the BV frequency of the  $1.6 M_\odot$  models with the two-zone modeling. These properties strongly motivate us to take the gradient in the

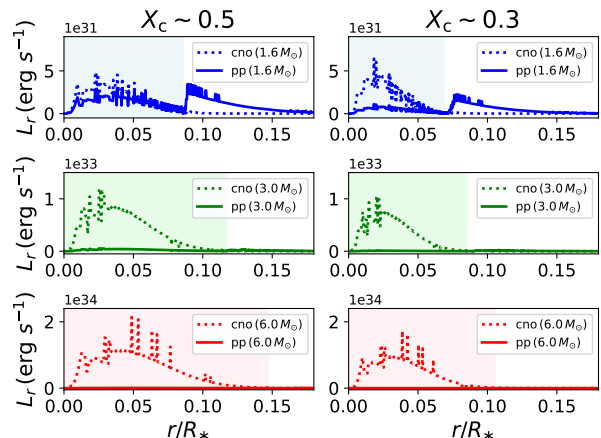


**Figure 2.** Nuclear energy generation rate  $L_r$  brought about by CNO cycle (dotted) or pp-chain reaction (solid) for various models with different masses and evolutionary stages (the same colors and columns, respectively, as in Figure 1). The horizontal axis shows the fractional radius, and the convective cores are indicated by shaded areas.

BV frequency into account in derivation of a new semi-analytical expression of the  $\Delta P_g$  pattern.

A possible origin for the mass-dependent sharpness of the BV frequency transition is the balance between two kinds of hydrogen burning mechanisms, namely, CNO cycle and pp-chain reaction (e.g. Kippenhahn et al. 2013). Figure 2 shows the nuclear energy generation rate, which is proportional to the amount of conversion from hydrogen to helium per second, brought about by CNO cycle (dotted) and pp-chain reaction (solid) for the stellar models. We clearly see that pp-chain reaction becomes more and more dominant over CNO cycle as the mass of the models decreases. Interestingly, in the case of  $1.6 M_\odot$  models, pp-chain cycle is at work across the edge of the convective-core boundary (see around the outer edge of the shaded area in the top panels of Figure 2), which smoothens the chemical composition gradient developed just above the convective core and renders the BV frequency transition milder as seen in the bottom panels of Figure 1.

As a final remark in this section, we point out that the sharpness of the BV frequency transition depends on the stellar evolutionary stage as well (compare left and right at the bottom panels of Figure 1), although it is not so evident as the mass dependence. Such age dependence is confirmed even for the  $6 M_\odot$  models, and thus, it should not be solely caused by the balance between the CNO cycle and pp-chain reaction. One possibility is that elemental diffusion processes have been smoothening the chemical composition gradient inside older stars for longer times, leading to a larger scale height of the

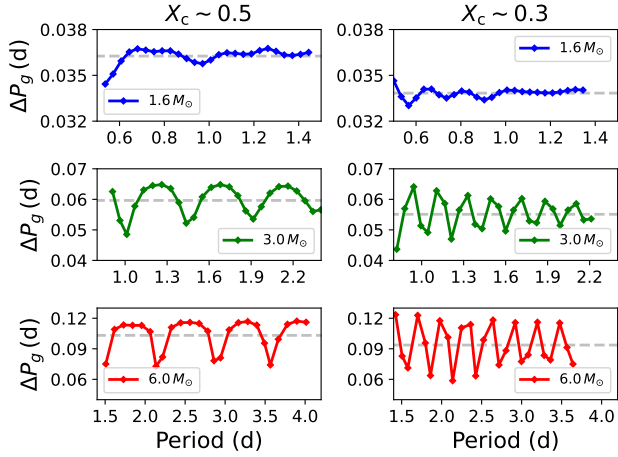


**Figure 3.** G-mode period spacings  $\Delta P_g$  against the g-mode periods that are numerically computed based on various models with different masses and evolutionary stages (the same colors and columns, respectively, as in Figure 1). Note that the scales of the vertical axes are different depending on the mass of the models; the amplitude of an oscillatory component in a  $\Delta P_g$  pattern is larger for massive models.

BV frequency  $H_N$ . Combined with the assumption that the typical wavelength of a high-order g mode ( $\lambda_g$ ) with a certain radial order  $n$  is not so changed as the star evolves, the smaller  $\lambda_g/H_N$  for the older models can be explained by their larger  $H_N$ . We will find the age dependence as well later in Section 4,

### 2.3. $\Delta P_g$ patterns of the models

In this section, we present  $\Delta P_g$  patterns which are numerically computed based on the stellar models discussed in the previous section. The linear adiabatic oscillation code GYRE (Townsend and Teitler 2013) is used, and eigenperiods of high-order ( $-40 < n < -13$ ) and dipole ( $l = 1$ ) g modes, which are theoretically predicted to be excited in main-sequence g-mode pulsators (Moravveji 2016), are calculated for each model.

Figure 3 shows the  $\Delta P_g$  patterns of the models thus computed. In all the cases, we see oscillatory behaviors in the  $\Delta P_g$  patterns. It is also seen that the mean value of the  $\Delta P_g$  pattern (dashed grey lines in Figure 3) becomes smaller as the model becomes older (compare the left and right panels).

One significant difference is the amplitude of the oscillatory component in the  $\Delta P_g$  pattern; the amplitude becomes larger as the model becomes more massive (note that the scales of the vertical axes are different in Figure 3). This corresponds to the fact that, as discussed in the previous section, a more massive model has a sharper BV frequency transition (see bottom row in Fig-

ure 1), resulting in a larger amplitude in the  $\Delta P_g$  pattern, which is consistent with the theoretical prediction (e.g. Miglio et al. 2008)

Another important point is that, especially in the cases of  $1.6 M_\odot$  and  $3.0 M_\odot$  models, we find that the amplitude becomes smaller as the g-mode period becomes longer. This is mainly because the ratio  $\lambda_g/H_N$ , which represents the degree of the BV frequency transition sensed by typical g modes, is proportional to the g-mode angular frequency  $\omega$  (see the numerator of Equation 2). The ratio  $\lambda_g/H_N$  is therefore smaller for a g mode with a longer period, leading to a smaller amplitude of the oscillatory component in the  $\Delta P_g$  pattern, which finally becomes zero in the asymptotic limit. Such a period dependence of the amplitude of the oscillatory  $\Delta P_g$  pattern has been pointed out by numerous authors from the theoretical point of view (e.g. Miglio et al. 2008; Cunha et al. 2019; Wu et al. 2020) although there so far has not been an explicit expression that reproduces the period dependence, which is another motivation for us to derive a new semi-analytical expression of the  $\Delta P_g$  pattern as we see in the next section.

## 3. SEMI-ANALYTICAL EXPRESSION OF $\Delta P_G$ PATTERN

As we see in Section 2, the BV frequency transition (between the large- $N$  and small- $N$  regions) becomes milder for less massive stars, which leads to the period dependence of the amplitude of an oscillatory component in the  $\Delta P_g$  pattern. Such a milder BV frequency transition can also prevent us from parameterizing the BV frequency of less massive stars with the two-zone modeling as has been conducted by Cunha et al. (2019). In this section, as an alternative way to model the BV frequency profile of less massive stars, we propose to parameterize the BV frequency with a ramp function based on which a semi-analytical expression of the  $\Delta P_g$  pattern is derived. We firstly review Cunha et al. (2019) to highlight a basic concept in our formulation (Section 3.1). Then, a new semi-analytical expression is given (Section 3.2). Finally, the derived expression will be validated (Section 3.3).

### 3.1. Revisiting Cunha et al. (2019)

There are two mainstreams in analytical studies of high-order g modes under the existence of the sharp variation in the BV frequency. In one approach, the sharp variation is considered as a perturbation to the BV frequency, and the  $\Delta P_g$  pattern is expressed as a result of the perturbed g-mode periods (the perturbative approach; Montgomery et al. 2003; Miglio et al. 2008; Wu et al. 2020). In the other approach, the eigenvalue

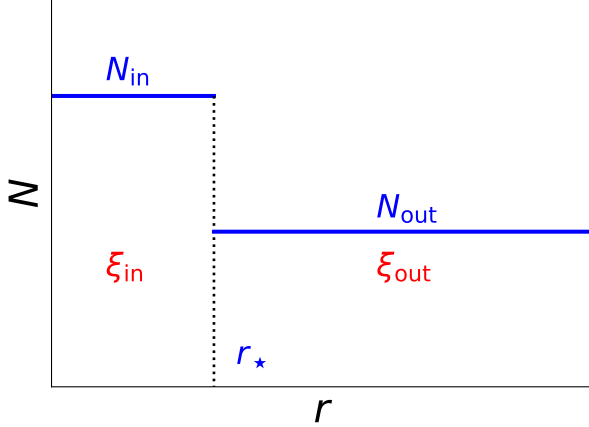


**Figure 4.** Schematic view of the two-zone modeling of the BV frequency  $N$  in the g-mode cavity, where the horizontal axis is the radius  $r$ . The BV frequency profile is modeled with the three parameters, namely, the value of the BV frequency in the inner region  $N_{\text{in}}$ , that in the outer region  $N_{\text{out}}$ , and the location of the discontinuity  $r_*$ . The eigenfunctions for the inner and outer regions are denoted by  $\xi_{\text{in}}$  and  $\xi_{\text{out}}$ , respectively.

condition is derived by linking a few JWKB solutions, enabling us to compute the explicit expression of the  $\Delta P_g$  pattern (e.g. Miglio et al. 2008; Cunha et al. 2015, 2019). Let us call the latter approach as the “direct” approach. Generally speaking, the perturbative approach is applicable for any variation with arbitrary shapes as long as the variation is small enough that it can be considered as a small perturbation. In contrast, the “direct” approach can only be used for a variation with a rather simple structure, but we do not have to assume that it is small. One of the reasons why Cunha et al. (2019) utilized the “direct” approach may be that we often find a fairly sharp BV frequency transition inside stellar models of main-sequence g-mode pulsators; it is not reasonable to consider the sharp variation in the BV frequency to be a small perturbation. In the same spirit as Cunha et al. (2019), we would like to focus on the “direct” approach, and we will briefly present the formulation by Cunha et al. (2019) below.

The starting point is the two-zone modeling of the BV frequency whose inner and outer edges are here assumed to be identical to those of the mode cavity of high-order g modes. Let us denote the inner and outer edges by  $r_0$  and  $r_1$ , respectively. The g-mode cavity is divided into two regions by a discontinuity in the BV frequency located at  $r = r_*$  (Figure 4).

What we would like to solve is the second-order differential equation for the high-order g modes (see, e.g.,

Gough 1993):

$$\frac{d^2\xi}{dr^2} + k_r^2\xi = 0, \quad (4)$$

where the eigenfunctions are represented by  $\xi$ . It is assumed that the local wavenumber  $k_r \sim LN/\omega r$  in which  $L^2 = l(l+1)$  following the notation of Cunha et al. (2019). Then, eigenfunctions for the inner and outer regions may be given based on the assumption of the Cowling approximation and JWKB approximation (see, e.g., Gough 1993). Below are the explicit forms of the eigenfunctions:

$$\xi_{\text{in}} = \tilde{\xi}_{\text{in}} \frac{1}{\sqrt{k_{\text{in}}}} \sin\left(\int_{r_0}^r k_{\text{in}} dr + \frac{\pi}{4}\right), \quad (5)$$

and

$$\xi_{\text{out}} = \tilde{\xi}_{\text{out}} \frac{1}{\sqrt{k_{\text{out}}}} \sin\left(\int_r^{r_1} k_{\text{out}} dr + \frac{\pi}{4}\right), \quad (6)$$

where  $k_{\text{in}}$  and  $k_{\text{out}}$  are the local wavenumbers in the inner and outer regions, respectively. There are constants related to the amplitudes of the eigenfunctions,  $\tilde{\xi}_{\text{in}}$  and  $\tilde{\xi}_{\text{out}}$ .

The next thing to do is to link the inner and outer eigenfunctions continuously and smoothly. The conditions can be expressed as the following boundary conditions at the discontinuity  $r = r_*$ :

$$\xi_{\text{in}}(r_*) = \xi_{\text{out}}(r_*), \quad (7)$$

and

$$\left. \frac{d\xi_{\text{in}}}{dr} \right|_{r=r_*} = \left. \frac{d\xi_{\text{out}}}{dr} \right|_{r=r_*}, \quad (8)$$

with which the constants  $\tilde{\xi}_{\text{in}}$  and  $\tilde{\xi}_{\text{out}}$  can be eliminated. After some manipulation (with the assumption that the first derivative of the local wavenumber can be neglected), we end up with the eigenvalue condition in the presence of a discontinuity in the BV frequency (Equation A6 in Cunha et al. 2019):

$$\begin{aligned} & \sin\left(\int_{r_0}^{r_1} k_r dr + \frac{\pi}{2}\right) = \\ & -A_* \sin\left(\int_{r_*}^{r_1} k_{\text{out}} dr + \frac{\pi}{4}\right) \cos\left(\int_{r_0}^{r_*} k_{\text{in}} dr + \frac{\pi}{4}\right), \end{aligned} \quad (9)$$

where the strength of the discontinuity is represented by  $A_*$  defined as below:

$$A_* \equiv \frac{k_{\text{in}}^* - k_{\text{out}}^*}{k_{\text{out}}^*}, \quad (10)$$

in which the local wavelength at the location of the discontinuity for the inner (outer) region is denoted by  $k_{\text{in}}^*$  ( $k_{\text{out}}^*$ ).

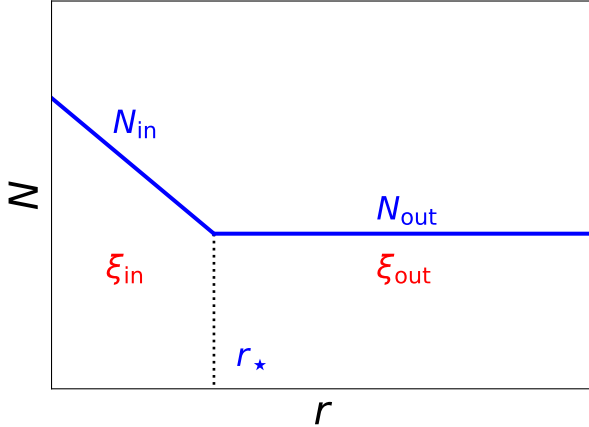


**Figure 5.** Schematic view of the BV frequency  $N$  whose inner region is modeled with a ramp. The variables have the same meaning as in Figure 4.

With some special techniques developed by Christensen-Dalsgaard (2012) (see also Cunha et al. 2015), the eigenvalue condition can be further analyzed, finally leading to the semi-analytical expression of the  $\Delta P_g$  pattern in the case of the two-zone modeling of the BV frequency (Cunha et al. 2019):

$$\frac{\Delta P_g}{\Delta P_{as}} \sim \left[ 1 - \left( \frac{\Pi_0}{\Pi_\star} \right) \frac{-A_\star \sin \tilde{\beta}_1 + A_\star^2 \cos^2 \tilde{\beta}_2}{(1 + A_\star \cos^2 \tilde{\beta}_2)^2 + (0.5 A_\star \cos \tilde{\beta}_1)^2} \right]^{-1}, \quad (11)$$

where the buoyancy radius  $\Pi_r^{-1}$  is defined as:

$$\Pi_r^{-1} = \int_{r_0}^r \frac{N}{r} dr, \quad (12)$$

with which  $\Pi_0^{-1} = \Pi_r^{-1}(r_1)$ ,  $\Pi_\star^{-1} = \Pi_r^{-1}(r_\star)$ , and  $\Delta P_{as} = 2\pi^2 \Pi_0 / L$ . The phases  $\tilde{\beta}_1$  and  $\tilde{\beta}_2$  inside the sinusoidal components in the equation above are defined as

$$\tilde{\beta}_1 = \frac{2L}{\omega} \Pi_\star^{-1} + 2\delta, \quad (13)$$

and

$$\tilde{\beta}_2 = \frac{L}{\omega} \Pi_\star^{-1} + \frac{\pi}{4} + \delta, \quad (14)$$

respectively. The extra phase term represented by  $\delta$  is necessary to quantify the phase jump produced around the boundaries of the g-mode cavity. See Cunha et al. (2015, 2019) for more discussions.

It should be instructive to mention that Equation (11) contains two essential properties expected for the  $\Delta P_g$  pattern, namely, that the amplitude and period of an oscillatory component in the  $\Delta P_g$  pattern are determined by the strength ( $A_\star$ ) and location ( $\Pi_\star^{-1}$ ) of the discontinuity, respectively.

### 3.2. A new formulation

In this section, a semi-analytical expression of the  $\Delta P_g$  pattern, for which the gradient in the BV frequency is taken into account, will be derived based on the “direct” approach (Section 3.1).

Our starting point is to model the BV frequency with a ramp (Figure 5). In this model, the outer edge of the ramp is defined as the location  $r_\star$  that divides the inner and outer regions as we see in Figure 5; we are thus focusing on a discontinuity in not the BV frequency but the first derivative of the BV frequency. In both regions, the corresponding eigenfunctions are assumed to be given by the JWKB solutions (Equations 5 and 6). This assumption seems to be too much of simplification, but it can be validated by remembering discussions in Chapter 16 of Unno et al. (1989) where a criterion for whether asymptotic analysis of high-order modes can be used or not has been indicated. We will discuss this point in the next two paragraphs.

One important quantity is  $\zeta$  which is related to the buoyancy frequency and is defined as below (see also Equation 16.22 in Unno et al. 1989):

$$\zeta = \text{sgn}(k_r^2) \left( \left| \frac{3}{2} \int_{r_0}^r |k_r| dr \right| \right)^{2/3}, \quad (15)$$

where we denote the sign function by  $\text{sgn}(\cdot)$ . The eigenfunctions of high-order g modes, which are solutions for the second-order differential equation formulated under the Cowling approximation (see, e.g., Unno et al. 1989), can be expressed by a linear combination of Airy functions when the following condition is satisfied:

$$\zeta \gg f \left( \frac{dr}{d\zeta} \right), \quad (16)$$

with the function  $f$  defined as (see also Equation 16.13 in Unno et al. 1989)

$$f(x) \equiv |x|^{1/2} \frac{d^2|x|^{-1/2}}{d\zeta^2}. \quad (17)$$

Note that eigenfunctions represented by the Airy function are asymptotically identical to the JWKB solutions for regions far from the turning point of the Airy function; we can thus use JWKB solutions as eigenfunctions for regions far from the edges of the g-mode cavity where  $\zeta \gg f(dr/d\zeta)$ .

Keeping in mind the discussion above, we show comparisons of  $\zeta$  and  $f(dr/d\zeta)$  for two examples of the simple BV frequency model with a ramp (the bottom panel of Figure 6). It is seen that, in both examples, the condition (16) is mostly satisfied except for around the location of the discontinuity in the first derivative of the BV

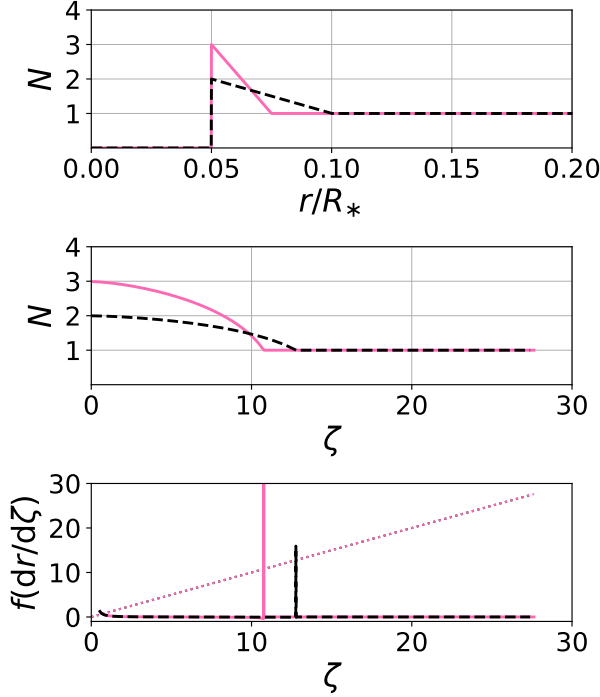


**Figure 6.** Two examples of BV frequency model with a ramp against the fractional radius (top), the same BV frequency profiles against  $\zeta$  (defined by Equation 15) (middle), and comparison between the corresponding  $f(dr/d\zeta)$  (solid and dashed curves) and  $\zeta$  (dotted lines) (bottom). See Equation (17) for the definition of the function  $f(\cdot)$ . Note that the BV frequencies are expressed in arbitrary units.

frequency ( $r \sim r_*$ ), which guarantees that we can safely use the JWKB solutions as the eigenfunctions for the inner and outer regions in the case of the BV frequency model with a ramp.

Once we determine the eigenfunctions for the inner and outer regions, we have to then consider the boundary conditions (7) and (8) to have the eigenvalue condition. It should be stressed that, since our BV frequency model is continuous elsewhere, the local wavenumbers are the same at the boundary ( $k_{\text{in}}^* = k_{\text{out}}^*$  at  $r = r_*$ ), and instead, the first derivative of the local wavenumber is discontinuous there. This is different from the two-zone model of Cunha et al. (2019) where the local wavenumber itself is discontinuous at the boundary.

We then have the eigenvalue condition in the case of the BV frequency model with a ramp:

$$\begin{aligned} & \sin\left(\int_{r_0}^{r_1} k_r dr + \frac{\pi}{2}\right) = \\ & - A'_* k_*^{-1} \sin\left(\int_{r_*}^{r_1} k_{\text{out}} dr + \frac{\pi}{4}\right) \sin\left(\int_{r_0}^{r_*} k_{\text{in}} dr + \frac{\pi}{4}\right), \end{aligned} \quad (18)$$

where the strength of the discontinuity (in the first derivative of the local wavenumber)  $A'_*$  is defined as below:

$$A'_* \equiv k_*^{\frac{1}{2}} \left( \left. \frac{dk_{\text{in}}^{-\frac{1}{2}}}{dr} \right|_{*-} - \left. \frac{dk_{\text{out}}^{-\frac{1}{2}}}{dr} \right|_{*+} \right) \quad (19)$$

in which the first (second) term represents the value of the left (right) derivative at  $r = r_*$ . It might be worth mentioning that  $A'_*$  is related to the difference in the reciprocal of the local-wavenumber scale height and that  $k_*^{-1}$  is proportional to the local wavelength ( $\lambda_g$ ) at  $r = r_*$ . Thus, the term  $A'_* k_*^{-1}$  is similar to the ratio  $\lambda_g/H_N$  that is used as an indicator of the degree of the BV frequency transition sensed by g modes in Section 2.2.

One remarkable point about the eigenvalue condition (18) is that the term  $A'_* k_*^{-1}$  is inversely proportional to g-mode periods  $P$ . Therefore, for a fixed strength of the discontinuity in the first derivative of the BV frequency ( $A'_*$ ), the degree of the BV frequency transition sensed by g modes ( $A'_* k_*^{-1}$ ) becomes smaller as the g-mode period is longer. This feature is consistent with what we have seen in the  $\Delta P_g$  patterns of the low-mass ( $1.3 - 3 M_\odot$ ) main-sequence models in Section 2.3. A similar discussion on the period dependence of the amplitude of  $\Delta P_g$  patterns can be found in Appendix 1 in Cunha et al. (2019) where the variation in the BV frequency is assumed to be shaped like a Gaussian distribution.

By using the techniques of Christensen-Dalsgaard (2012) in the same way as in Cunha et al. (2019), we can derive a semi-analytical expression of the  $\Delta P_g$  pattern that takes into account the gradient in the BV frequency. The explicit expression is actually the same as Cunha et al.'s original one (11) except that the constant  $A_*$  is replaced with the period-dependent term  $A'_* k_*^{-1}$ .

### 3.3. Validity check of the derived expression

In this section, validity check of the semi-analytical expression derived in the last section is conducted. To this end, using some simple artificial BV frequency profiles, we have compared  $\Delta P_g$  patterns analytically computed (with the semi-analytical expression) and those numerically computed.

We start with somewhat an ordinary case (Section 3.3.1) in a sense that the strength of the discontinuity in the first derivative of the artificial BV frequency ( $A'_*$ ) is comparable to that of the stellar models computed in Section 2.2. Then, we move on to the case where the variation in the BV frequency can be treated as a small perturbation (Section 3.3.2), where g-mode period spacings computed based on the first order perturbation



theory is compared as well. Note that, in both cases, the gradient in the BV frequency is set to be constant with respect not to the fractional radius but to the buoyancy radius. This enables us to use the analytical expression of the  $\Delta P_g$  pattern derived based on the perturbative approach, which is especially relevant in Section 3.3.2. Note also that we are considering only dipole modes ( $l = 1$ ) in this section.

### 3.3.1. When the variation in the BV frequency cannot be treated as a small perturbation

The top panel of Figure 7 shows the BV frequency model based on which  $\Delta P_g$  patterns are to be semi-analytically/numerically computed in this subsection. The ratio between the value of the BV frequency at the innermost point ( $r/R_* \sim 0.1$ ) and that of the outer region ( $r/R_* > 0.125$ ) is determined so that it is close to typical values in the case of ordinary stellar models (see Figure 1).

The “numerical”  $\Delta P_g$  pattern is calculated by numerically solving the second-order differential equation (4) with simple boundary conditions, namely,  $\xi = 0$  at the center and  $d\xi/dr = 0$  at the surface. Then subtraction has been taken between the eigenperiods with the neighboring radial orders ( $n + 1$  and  $n$ ) to obtain the g-mode period spacings  $P_{n+1} - P_n$ . As for the “semi-analytical”  $\Delta P_g$  pattern, the parameters  $\Pi_0$ ,  $\Pi_*$ ,  $A'_*$ , and  $k_*^{-1}$ , which are directly extracted from the prepared BV frequency profile, are substituted for the explicit expression (11) (please keep in mind that the constant  $A_*$  should be replaced with the period-dependent term  $A'_* k_*^{-1}$ ). The numerically computed eigenfrequencies  $\omega$  are used in the phase terms (13) and (14). Note that  $\delta$  in these phase terms are treated as a free parameter whose value is determined so that the phase of the oscillatory component in the “semi-analytical”  $\Delta P_g$  pattern matches that in the “numerical”  $\Delta P_g$  pattern.

In the bottom panel of Figure 7, the “numerical” and “semi-analytical”  $\Delta P_g$  patterns thus obtained are compared, which clearly shows a fairly good agreement between them. We especially would like to emphasize that the “semi-analytical”  $\Delta P_g$  patterns can successfully reproduce the period dependence of the amplitude of the oscillatory component in the “numerical”  $\Delta P_g$  patterns; the amplitude becomes smaller as the g-mode period becomes longer.

### 3.3.2. When the variation in the BV frequency can be treated as a small perturbation

Although it is generally considered that the strength of the discontinuity in the first derivative of the BV frequency ( $A'_*$ ) in ordinary main-sequence g-mode pulsators is not so small that we cannot treat it as a small

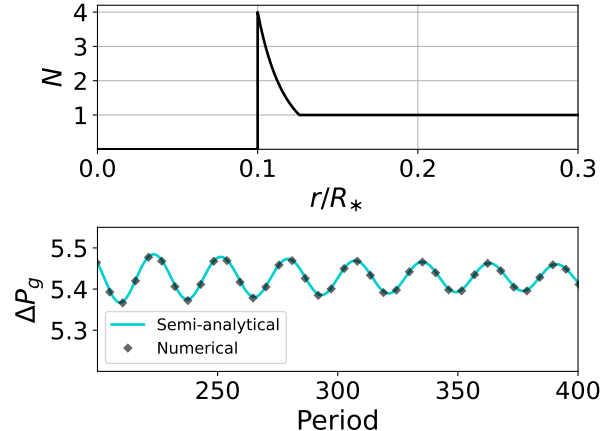


**Figure 7.** Simple artificial model of the BV frequency with a ramp (top), based on which the “numerical” and “semi-analytical”  $\Delta P_g$  patterns have been computed (dark grey diamond and light blue curve, respectively, in the bottom panel). The BV frequency is expressed in arbitrary units, and so are the g-mode periods and  $\Delta P_g$  patterns. Note that the gradient in the BV frequency is constant with respect to the buoyancy radius.

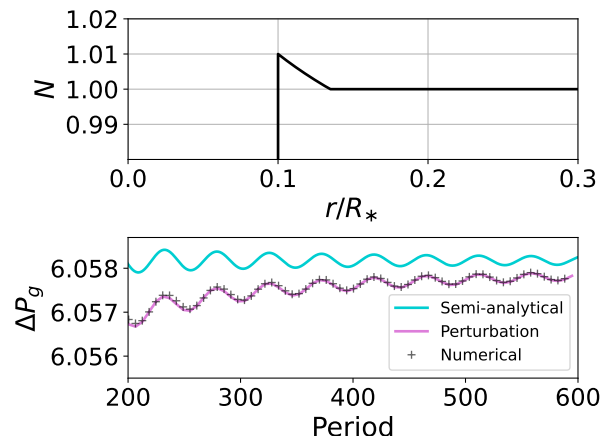


**Figure 8.** Same as Figure 7 except that the variation in the BV is modeled as a small perturbation. The  $\Delta P_g$  pattern calculated based on the perturbative approach (pink curve in the bottom panel) are shown in addition to the “numerical” (black crosses) and “semi-analytical” (light blue curve)  $\Delta P_g$  patterns.

perturbation (see discussions in Section 2.2), the perturbative approach (e.g. Miglio et al. 2008) is still quite useful for validating the derived semi-analytical expression since another analytical expression of the  $\Delta P_g$  pattern can relatively readily be obtained based on the perturbative approach (see Appendix A).

Figure 8 shows a BV frequency model with a tiny ramp (top) and “numerical”, “semi-analytical”, and “perturbative”  $\Delta P_g$  patterns (black crosses, light blue curve, and pink curve, respectively, in the bottom

panel). We have followed the same steps as described in the last subsection to compute the “numerical” and “semi-analytical”  $\Delta P_g$  patterns. The “perturbative”  $\Delta P_g$  pattern is calculated based on Equation (A3), in which the g-mode periods numerically computed based on the corresponding unperturbed BV frequency are used for  $P_n$  in the expression.

We have again found a good agreement among the  $\Delta P_g$  patterns thus computed, especially regarding the trend that the amplitude of the oscillatory component in the  $\Delta P_g$  pattern decreases with the g-mode periods. (Notice that the scale is significantly different from that in the bottom panel of Figure 7.) It should be mentioned that there exist some offsets between the “semi-analytical” and the other  $\Delta P_g$  patterns. This may arise from the fact that the local wavenumber  $k_r$  is proportional to  $r^{-1}$ , which renders  $k_r$  to be significantly large around the central region ( $r \sim 0$ ), affecting relatively low-order (or shorter-period) modes and resulting in a phenomena somewhat similar to mode trapping. But such effect has not been taken into account in the derivation of the semi-analytical expression, which may cause the offsets between the “semi-analytical” and the other  $\Delta P_g$  patterns. We nevertheless would like to emphasize that the offsets approach zero as we see the  $\Delta P_g$  patterns in the higher g-mode period range than that shown in the bottom panel of Figure 8.

#### 4. APPLICATION

In this section, we would like to assess how applicable the new semi-analytical expression of the  $\Delta P_g$  pattern is for studying the BV frequency profile of main-sequence g-mode pulsators. We firstly attempt to fit the semi-analytical expression to  $\Delta P_g$  patterns of realistic stellar models in order to investigate to what extent we can accurately extract the information on the BV frequency transition inside the stellar models using the semi-analytical expression (Section 4.1). Then, as an example to highlight the usefulness of the semi-analytical expression, a case study of the fitting procedure for one of the Kepler targets, KIC 11145123, is given (Section 4.2).

##### 4.1. Attempts to fit the semi-analytical expression to $\Delta P_g$ patterns of stellar models

The goal of this section is to compare two sets of parameters that describe the BV frequency model with a ramp (see Section 3.2 for definitions of the parameters). One is the set of parameters directly extracted from stellar models, and the other is that estimated by fitting the semi-analytical expression to the  $\Delta P_g$  patterns numerically computed with the stellar models. After

presenting stellar models used in this section and how to extract the parameters from the models (Subsection 4.1.1), artificial  $\Delta P_g$  patterns to be fitted are generated in Subsection 4.1.2. A fitting procedure is given in Subsection 4.1.3, based on which parameters are estimated and finally compared with those directly extracted from the stellar models (Subsection 4.1.4).

##### 4.1.1. Stellar models and how to extract parameters

Based on the same settings as described in Section 2.1, we have computed 1.6, 2, 3, and  $4 M_\odot$  models with various evolutionary stages represented by the hydrogen mass content at the center  $X_c \sim 0.5, 0.4, 0.3,$  and  $0.2$ .

For later use in Subsection 4.1.4, we then have to extract the parameters from these models (see Section 3.2 for the definitions), which is, however, not a straightforward thing to do. This is because the location of the outer edge of the ramp in the BV frequency ( $r_\star$ ) is not obvious at all; although the location  $r_\star$  is defined to be where the first derivative of the BV frequency is discontinuous in the case of the simple model of the BV frequency with a ramp, there is no such discontinuity in realistic stellar models. Then, where should the location  $r_\star$  be? Similarly, how should we compute the strength of the discontinuity (in the first derivative of the local wavenumber)  $A'_\star$ ? We would like to articulate these points in the following paragraphs.

The first parameter to be discussed is the location of the outer edge of the ramp  $r_\star$ . A hint for where it should be in the case of a stellar model can be obtained by remembering the discussions in Section 3.2. The important point is that  $r_\star$  corresponds to where  $f(dr/d\zeta)$  is maximum (see Figure 6). As shown in Figure 9, in the case of realistic stellar models,  $f(dr/d\zeta)$  is closely related to  $A'$  that is defined as

$$A' \equiv \frac{d \ln k_r^{-\frac{1}{2}}}{dr}. \quad (20)$$

This is reasonable since  $f(dr/d\zeta)$  is essentially related to the second derivative of the local wavenumber  $k_r$  (see Equation 17) while  $A'$  contains the first derivative of  $k_r$ . Accordingly, when we focus on a region where the gradient of the BV frequency is steep (see around  $0.10 < r/R_\star < 0.11$  in Figure 9), we find that the position of the local maximum of  $f(dr/d\zeta)$  is almost identical to that of the local minimum of the first derivative of  $A'$  (see the yellow shaded areas in Figure 9). We are thus going to define  $r_\star$  as the position where the first derivative of  $A'$  is locally minimum in the rest of this paper. (For example, in the case of Figure 9,  $r_\star \sim 0.111$ .)

The next parameter to be discussed is the strength of the discontinuity in the first derivative of the local

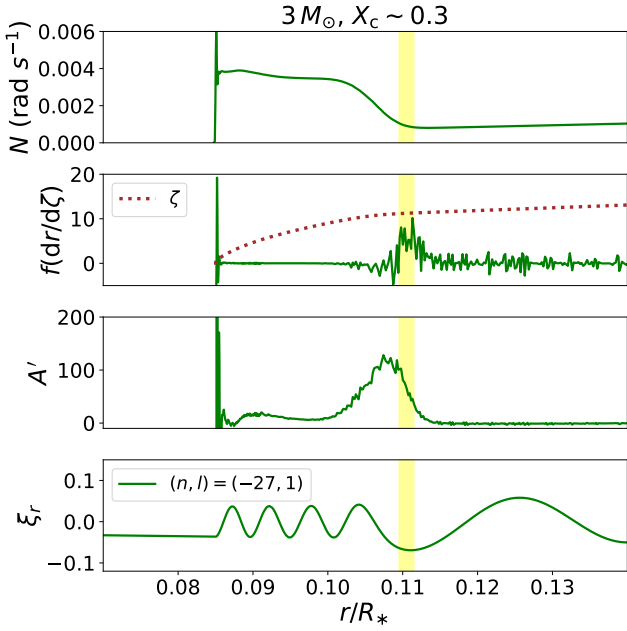


**Figure 9.** Internal properties around the deep radiative region of the  $3 M_{\odot}$  model with the central hydrogen mass content  $X_c \sim 0.3$ . From top to bottom, the BV frequency profile, the comparison of  $f(dr/d\zeta)$  (green curve) and  $\zeta$  (red dotted curve), the parameter  $A'$ , and the radial component of a g-mode eigenfunction with  $(n, l) = (-27, 1)$  are shown in this order. The horizontal axis is the fractional radius  $r/R_*$ , and the relevant range is common to all the panels. Yellow shaded areas indicate where the outer edge of the BV frequency ramp is located. Definitions of the parameters and how we decide the location of the outer edge of the ramp can be found in the text.

wavenumber ( $A'_*$ ). In Section 3.2,  $A'_*$  is defined as the subtraction between left and right derivatives at  $r = r_*$  (see Equation 19) because the first derivative of the local wavenumber  $k_r$  is discontinuous there. This is in contrast not the case for a stellar model where  $dk_r/dr$  is continuous in the deep radiative region (see discussions in Section 2.2). We thus have to take subtraction for a certain interval; how should we determine the interval then?

The point is how high-order g modes sense the sharp variation in the first derivative of  $k_r$ , which should be determined by the ratio between a width, with which the sharp variation in the first derivative of  $k_r$  occurs, and a typical local wavelength of the high-order g modes. Figure 9 shows that the width (in which  $f(dr/d\zeta) \sim \zeta$ ) is much smaller than the wavelength of a typical high-order g mode. It is thus expected that the high-order g modes should sense the sharp variation (in the first derivative of  $k_r$ ) as a rather “abrupt” change in the structure. Together with the fact that  $A'_* \sim [A']_{*+}^* -$  (see Equations 19 and 20), we choose to define  $A'_*$  as the difference between

the local maximum and local minimum of  $A'$  that are found in a certain section around the outer edge of the BV frequency ramp ( $r \sim r_*$ ). The section is defined so that its center and width are identical to the location  $r_*$  and one local wavelength of the typical g mode, respectively. (For instance, in the case of Figure 9, the local maximum and local minimum of  $A'$  found in a section around  $r \sim r_*$  are about  $\sim 120$  and  $\sim 0$ , respectively, leading to  $A'_* \sim 120$ .)

All the parameters in the semi-analytical expression of the  $\Delta P_g$  pattern can be computed based on the redefinitions demonstrated above. These ways of redefining the parameters, which appear to be ad hoc, will be validated later in Subsection 4.1.4. Note that the extra phase term  $\delta$  is treated as a free parameter to be fitted in this study, and we are not going to discuss it in detail.

#### 4.1.2. How to generate artificial $\Delta P_g$ patterns to be fitted

For artificial datasets, we have numerically computed g-mode periods and  $\Delta P_g$  patterns with the stellar models that are calculated in the previous subsection. The frequency computation has been carried out based on the same settings as described in Section 2.2. To mimic observational uncertainties, random numbers are added to the  $\Delta P_g$  patterns, where they are assumed to follow the Gaussian distribution with the mean and standard deviation equal to 0 and  $10^{-4}$  (in units of day), respectively, and they are statistically independent of each other. The value of the standard deviation is determined based on typical observational uncertainties of  $\Delta P_g$  patterns (e.g. Papics et al. 2014; Van Reeth et al. 2015).

#### 4.1.3. Fitting procedure

We conduct the fitting to the artificial datasets via the Metropolis method (Metropolis et al. 1953), which is one of the standard techniques to carry out Markov chain Monte Carlo (MCMC) sampling (see, e.g., Gregory 2005). Parameters to be estimated are as follows (see also Sections 3.1 and 3.2): the buoyancy radius at the outer edge of the g-mode cavity ( $\Pi_0$ ), that at  $r = r_*$  ( $\Pi_*$ ), the extra phase term ( $\delta$ ), and the degree of the structural variation ( $B_*$ ) which is defined so that  $A'_* k_*^{-1} = P^{-1} B_*$ . The final parameter has been introduced by assuming that the term  $A'_* k_*^{-1}$  is inversely proportional to the g-mode period ( $P$ ), which is correct when we neglect the period dependence of  $A'_*$  (we will discuss the point later in Subsection 4.1.4). Introducing the parameter is also helpful since it prevents us from suffering from degeneracies among parameters such as  $A'_*$ ,  $r_*$ , and  $N_*$ . From now on, we will denote by  $\theta$  the set of the parameters to be estimated.

The likelihood of the parameter set  $\theta$  given a certain g-mode period spacing  $\Delta P_i^{\text{obs}}$  is here defined in the following way:

$$p(\Delta P_i^{\text{obs}}|\theta) = \frac{1}{\sqrt{2\pi}e_i} \exp\left[-\frac{1}{2}\left(\frac{\Delta P_i^{\text{obs}} - \Delta P_i^{\text{mod}}(\theta)}{e_i}\right)^2\right], \quad (21)$$

where  $\Delta P_i^{\text{mod}}(\theta)$  is computed by substituting the parameter set  $\theta$  and corresponding g-mode period  $P_i^{\text{obs}}$  for the derived semi-analytical expression. The observational uncertainty  $e_i$  is assumed to be  $10^{-4}$  (in units of day). The data  $\Delta P_i^{\text{obs}}$  is statistically independent of each other so that the likelihood of the parameter set  $\theta$  given a certain dataset  $\Delta \mathbf{P}^{\text{obs}}$  can be expressed as below:

$$p(\Delta \mathbf{P}^{\text{obs}}|\theta) = \prod_{i=1}^{N_{\text{obs}}} p(\Delta P_i^{\text{obs}}|\theta). \quad (22)$$

The number of data used for fitting is denoted by  $N_{\text{obs}}$ .

With the likelihood (22) as well as prior probabilities of the parameters which are assumed to be uninformative to be uniform, we have carried out the Metropolis method to sample the posterior probability distribution of the parameters. A typical number of iterations for the sampling processes to converge and that of the so-called burn-in period (during which the obtained samples are not thought to be realizations from the posterior probability distribution) are about  $5 \times 10^5$  and  $10^5$ , respectively. Convergence of the sampling has been confirmed by visual inspection.

#### 4.1.4. Parameter estimation and comparison

For each of the artificial datasets which can be labeled by the mass ( $M$ ) and central hydrogen mass content ( $X_c$ ) of the corresponding stellar model, we have carried out MCMC fitting based on the procedure described in the previous subsection. The means of the resultant posterior probability distribution functions are chosen as estimates of the parameters, namely,  $\Pi_0$ ,  $\Pi_*$ , and  $B_*$ , for each stellar model.

Table 1 shows relative differences between the estimates thus obtained and those directly extracted from the models. Note that the relative difference is defined as below:

$$\delta \ln q = \frac{\hat{q} - q_{\text{mod}}}{q_{\text{mod}}}, \quad (23)$$

where  $\hat{q}$  and  $q_{\text{mod}}$  represent an estimate of a particular parameter  $q$  and that directly extracted from a stellar model, respectively.

One remarkable point about the result of MCMC fitting is that parameter estimation works quite well

**Table 1.** Relative differences in the parameters,  $\Pi_0$  (top table),  $\Pi_*$  (middle table), and  $B_*$  (bottom table), between the estimates obtained via MCMC fitting and those directly extracted from the stellar models. Each element in the tables represents a relative difference in the corresponding parameter obtained in the case of a certain stellar model which is designated by the mass (row) and central hydrogen mass content (column). The relative difference is defined as equation (23), and it is expressed in units of %.

$\delta \ln \Pi_0$ (%)				
	$X_c \sim 0.5$	$X_c \sim 0.4$	$X_c \sim 0.3$	$X_c \sim 0.2$
$1.6 M_\odot$	-1.2	-1.3	-1.7	-2.3
$2 M_\odot$	-1.4	-1.3	-1.1	-0.83
$3 M_\odot$	-1.5	-1.5	-1.6	-1.6
$4 M_\odot$	-1.6	-1.7	-1.8	-2.4
$\delta \ln \Pi_*$ (%)				
	$X_c \sim 0.5$	$X_c \sim 0.4$	$X_c \sim 0.3$	$X_c \sim 0.2$
$1.6 M_\odot$	-4.6	-3.5	2.4	2.9
$2 M_\odot$	1.6	1.7	0.94	1.9
$3 M_\odot$	1.2	0.52	-0.020	1.5
$4 M_\odot$	1.1	1.9	0.89	0.48
$\delta \ln B_*$ (%)				
	$X_c \sim 0.5$	$X_c \sim 0.4$	$X_c \sim 0.3$	$X_c \sim 0.2$
$1.6 M_\odot$	-60	-55	-76	-86
$2 M_\odot$	-21	-36	-47	-57
$3 M_\odot$	14	-0.30	-7.5	-23
$4 M_\odot$	8.3	1.2	-8.5	-18

( $\delta \ln q \sim$  a few %) for the buoyancy radius at the outer edge of the g-mode cavity ( $\Pi_0$ ) and that at  $r = r_*$  ( $\Pi_*$ ), which is the case for almost all the stellar models considered in this section (see top and middle tables in Table 1). Some systematic underestimation of  $\Pi_0$  arise probably due to the factor  $r^{-1}$  in the local wavenumber  $k_r$  (see discussions in Section 3.3.2); the asymptotic value (1) is an upper bound for the corresponding  $\Delta P_g$  pattern numerically computed as we see in Figure 8.

As for the degree of the structural variation ( $B_*$ ), whether parameter estimation works well or not depends on the mass and central hydrogen mass content. We see that parameter estimation is rather accurate in the case of the 3 and  $4 M_\odot$  models; the relative differences are smaller than 25%, and they are especially small ( $< 10\%$ ) for the younger models (see the bottom table in Table 1), indicating the high potential of the semi-analytical approach to infer the degree of the structural variation inside, e.g., SPB or  $\beta$  Cep stars.

On the other hand, it is evident that estimating  $B_*$  is quite difficult for the less massive 1.6 and  $2 M_\odot$  models; a typical absolute value of the relative differences

is larger than 50%. Therefore, it might be impractical to apply the semi-analytical expression to less massive main-sequence g-mode pulsators such as  $\gamma$  Dor stars for inferring the degree of the structural variation inside them.

The tendency that inaccuracies in parameter estimation of  $B_\star$  become larger as a stellar model becomes less massive or older may arise from the assumption that we neglect the period dependence of  $A'_\star$  when we introduce  $B_\star$ . However, the interval for which the subtraction is taken (see Equation 19) should vary as the local wavelength of gravity waves changes;  $A'_\star$  is implicitly period-dependent. In particular, it is expected that the milder and wider the BV frequency transition is, the more relevant the local wavelength of gravity waves is in terms of how to define the width of the interval. In other words, the degree of the period dependence of  $A'_\star$  becomes larger for milder and wider BV frequency transitions. This is actually in accordance with the result that parameter estimation of  $B_\star$  does not work well for the less massive or older stellar models that exhibit milder and wider BV frequency transitions as discussed in Section 2.2 (see also Figure 1).

We could thus refine the semi-analytical expression by somehow taking into account the period dependence of  $A'_\star$ . Interestingly, we have seen a trend that we are more prone to underestimating  $B_\star$  as the star becomes older even for the massive models (though the values of  $\delta \ln B_\star$  is not so large), which could be resolved as well by the improvement suggested above. We will discuss the improvement in the forthcoming paper.

Finally, in order to check how well we can reproduce the  $\Delta P_g$  patterns of the stellar models, fitted  $\Delta P_g$  patterns are computed by inserting the so-called Maximum A Posteriori (MAP) estimator, which provides us with a parameter set that maximizes the posterior probability, into the semi-analytical expression. Figures 10 and 11 show comparisons of the fitted  $\Delta P_g$  patterns thus computed (colored curves) with those numerically computed (black diamonds) based on the 4 and  $2 M_\odot$  models, respectively, at two different evolutionary stages  $X_c \sim 0.4$  and 0.2.

In the cases of the  $4 M_\odot$  models (Figure 10), we see a fairly good agreement between the fitted and numerical  $\Delta P_g$  patterns, which is consistent with the result that parameter estimation works well for the relatively massive models. On the other hand, it is apparent in the cases of  $2 M_\odot$  models that the fitted  $\Delta P_g$  patterns cannot completely reproduce the numerical results (Figure 11), which may be related to the negligence of the implicit period dependence of  $A'_\star$  as we mentioned a few paragraphs before. It should especially be noted that

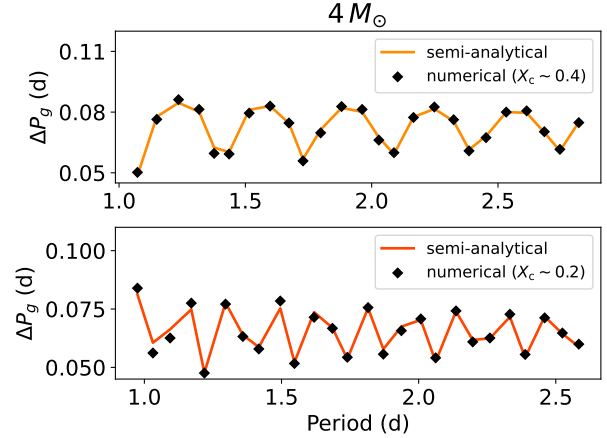


**Figure 10.** Comparison of the fitted  $\Delta P_g$  patterns (warm-color curves) with those numerically computed (dark grey diamonds) in the case of the  $4 M_\odot$  models with the central hydrogen mass content  $X_c \sim 0.4$  or 0.2 (top or bottom, respectively). The g-mode period (the abscissa) and its period spacing (the ordinate) are expressed in units of day.

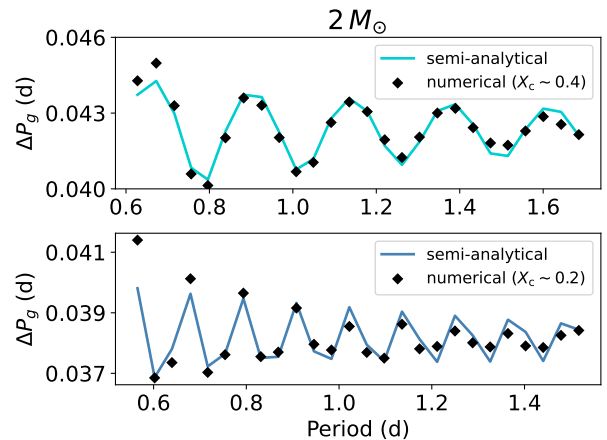


**Figure 11.** Same as Figure 10 in the case of the  $2 M_\odot$  models except that the fitted  $\Delta P_g$  patterns are shown in cool colors.

the amplitude of the oscillatory  $\Delta P_g$  pattern is overestimated (underestimated) for the shorter (longer) g-mode period (see Figure 11), indicating that the amplitude decreases more rapidly with respect to the g-mode period compared with what the semi-analytical expression predicts. Nevertheless, we also would like to stress that the semi-analytical expression at least succeeds in reproducing the decreasing amplitude of the oscillatory component in the  $\Delta P_g$  pattern against the g-mode period, which certainly is an advantage the semi-analytical expression derived in this study has.

#### 4.2. A case study of KIC 11145123

As another example of applications of the derived semi-analytical expression for the  $\Delta P_g$  pattern, we will present a case study where the expression has been fitted to the observed  $\Delta P_g$  pattern of one of the Kepler targets, KIC 11145123.

KIC 11145123 is a  $\delta$  Sct- $\gamma$  Dor hybrid pulsator observed by the Kepler probe for four years (Huber et al. 2014), so far found to be exhibiting 15 high-order ( $l = 1$ ) g modes, 2 low-order ( $l = 1$ ) p modes, and 6 ( $l = 2$ ) mixed modes (Kurtz et al. 2014). The observed  $\Delta P_g$  pattern has been used for carrying out asteroseismic modeling of the star (Kurtz et al. 2014; Takada-Hidai et al. 2017; Hatta et al. 2021), finding, for instance, that the star has exhausted almost all the hydrogen at the nuclear burning core (namely, that the star is at the terminal-aged main-sequence stage) and that the mass of the star is around  $1.4 M_\odot$ . Note also that the well-resolved rotational splitting of the star indicates that the star is a slow rotator with the rotation period of  $\sim 100$  days (e.g. Kurtz et al. 2014).

Interestingly, Hatta et al. (2021) have claimed that, in order to reproduce the observed  $\Delta P_g$  pattern of the star, the chemical composition gradient in the deep radiative region of the star should be much steeper than those of 1-dimensional evolutionary models in which mixing processes such as elemental diffusion and convective overshooting are treated basically with the default settings in MESA (see, e.g., Paxton et al. 2011, 2013, 2015, 2018, 2019). To emphasize the point, they have presented a seismic model of the star that is constructed by artificially increasing the chemical composition gradient just above the convective core of a  $1.4 M_\odot$  evolutionary model (see more details for Hatta et al. 2021).

Although the inferred mass of the star ( $\sim 1.4 M_\odot$ ) seems to be too small for us to apply the semi-analytical expression based on the result of Section 4.1, this is not the case. The reason is that the peculiarly sharp chemical composition gradient inferred based on the seismic model constructed by Hatta et al. (2021) can justify applying the derived semi-analytical expression to the star, which has motivated us to carry out the case study with the star in this section. It should also be noticed that the BV frequencies of the models have ramp structures (see top panel in Figure 12), preventing us from using the semi-analytical expression derived in Cunha et al. (2019).

We have followed the same procedure as described in Section 4.1 to fit the semi-analytical expression to the observed  $\Delta P_g$  pattern of the star. The values of the observed  $\Delta P_g$  spacings and the corresponding observational uncertainties can be found in Kurtz et al. (2014).

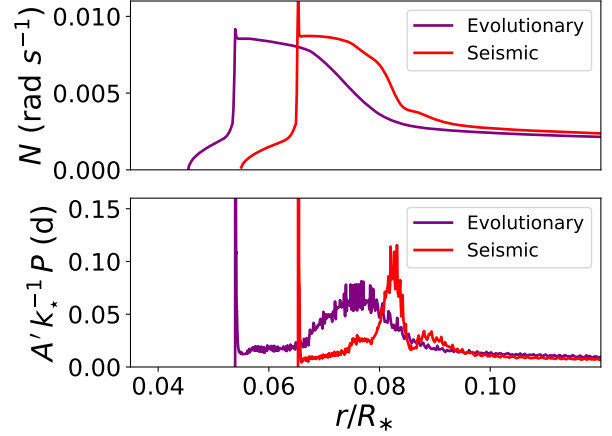


**Figure 12.** Structural parameters around the deep radiative region of the evolutionary (purple curves) and seismic (red curves) models of KIC 11145123 constructed by Hatta et al. (2021) via asteroseismic modeling. The top and bottom panels show BV frequency  $N$  and a parameter  $A'k_*^{-1}P$ , respectively, against the fractional radius  $r/R_*$ . Note that the degree of the structural variation ( $B_*$ ) can be expressed as  $B_* = [A'k_*^{-1}P]_*^{+}$ , and that we thus have to take subtraction between the maximum and minimum values of  $A'k_*^{-1}P$  to compute  $B_*$  (see also discussions in Section 4.1.1). Definitions of the parameters can be found in the text.

The estimate of the degree of the structural variation  $B_*$  thus obtained is  $0.093 \pm 0.002$  (in units of days) that is significantly larger than that of Hatta et al.’s  $1.4 M_\odot$  evolutionary model ( $B_* \sim 0.06$ ) (see the purple curve in the bottom panel of Figure 12, and take the difference between the “peak” and “baseline” values found around the sharp transition region. See also Section 4.1.1). We have thus confirmed that the degree of the structural variation  $B_*$  in the deep radiative region of the star should be significantly larger than that predicted based on ordinary 1-dimensional evolutionary computations, which is consistent with the argument of Hatta et al. (2021). Moreover, the estimate ( $B_* = 0.093 \pm 0.002$ ) is close to that directly extracted from the seismic model of Hatta et al. (2021) ( $B_* \sim 0.09$ ) (see the red curve in the bottom panel of Figure 12, and take the difference between the “peak” and “baseline” values found around the sharp transition region), clearly indicating that the seismic model is more favored than the original evolutionary model in terms of the observed  $\Delta P_g$  pattern of the star. The semi-analytical expression derived in Section 3 is thus shown to be quite useful in the case of the star.

The result that the fitting procedure works well for KIC 11145123 whose mass has been estimated to be around  $1.4 M_\odot$  seems to contradict with what we find in Section 4.1 that it is not appropriate to apply the semi-

analytical expression of the  $\Delta P_g$  pattern derived in Section 3 to lower-mass main-sequence g-mode pulsators. However, we would like to emphasize that the tests in Section 4.1 have been carried out based on the rather simple stellar models and that the most essential parameter that determines whether or not we can describe the  $\Delta P_g$  pattern with the semi-analytical expression is not the stellar mass but the degree of the sharp variation (in the first derivative of  $k_r$ ) inside a star (see discussions in Subsection 4.1.4). Therefore, in a sense, it may be such a coincidence that KIC 11145123 has a sharp structural variation in its deep radiative region whose degree is large enough that the semi-analytical expression is applicable. Related to this point, [Hatta et al. \(2021\)](#) have suggested that elemental diffusion much weaker than that predicted by ordinary 1-dimensional evolutionary codes can produce a steep chemical composition gradient (which leads to the large value of  $B_*$ ) even inside the low-mass main-sequence g-mode pulsators.

We finally show three  $\Delta P_g$  patterns, namely, the one observed for KIC 11145123, the one obtained by inserting the estimated parameters into the semi-analytical expression, and the one numerically computed based on the evolutionary  $1.4 M_\odot$  model of [Hatta et al. \(2021\)](#) (Figure 13). It is clearly seen that the fitted semi-analytical expression (turquoise curve) reproduces the amplitude of the oscillatory component in the observed  $\Delta P_g$  pattern (black dotted curve) much better than the  $\Delta P_g$  pattern of the  $1.4 M_\odot$  evolutionary model (purple curve). Note that there still exists a systematic deviation between the observed  $\Delta P_g$  pattern and the fitted semi-analytical one, which is thought to be caused by convective overshooting ([Hatta et al. 2021](#)). We will discuss the point in the next section as well as the effect of rotation.

## 5. DISCUSSION

We have seen that the semi-analytical expression derived in Section 3 is useful for studying the sharp BV frequency variation in intermediate-mass main-sequence g-mode pulsators ( $1.3 M_\odot < M < 4 M_\odot$ ) given that the degree of the variation is large enough to validate the assumptions adopted in the derivation of the semi-analytical expression (e.g. the condition 16). We then would like to remind the readers of another important assumption in the derivation of the semi-analytical expression, i.e., we neglect rotation and convective overshooting, both of which play important roles inside the intermediate-mass main-sequence g-mode pulsators ([Maeder 2009](#)). In this section, we give brief reviews and discussions about impacts rotation and convective overshooting have on  $\Delta P_g$  patterns.

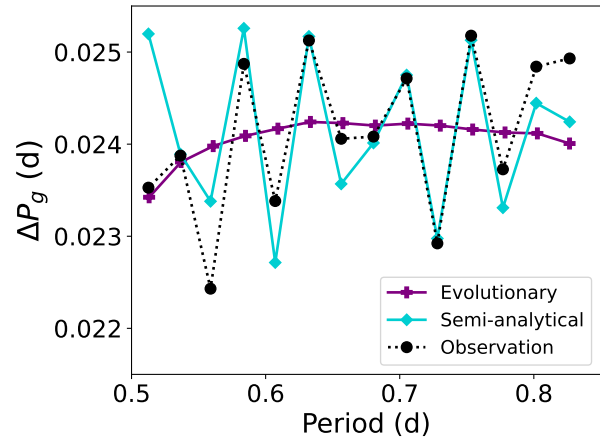


**Figure 13.** Comparison of the observed  $\Delta P_g$  pattern for KIC 11145123 (black dotted curve with circles), the fitted  $\Delta P_g$  pattern obtained with the semi-analytical expression (light blue curve with diamonds), and the  $\Delta P_g$  pattern numerically computed with the evolutionary model of [Hatta et al. \(2021\)](#) (purple curve with crosses). The g-mode period (the abscissa) and its period spacing (the ordinate) are expressed in units of day. Note that the observational uncertainties of the  $\Delta P_g$  spacings ( $\sim 10^{-5}$  in units of days) are much smaller than the size of the markers.

It is generally considered that early-type stars are rotating rapidly ( $v \sin i \sim$  one hundred  $\text{km s}^{-1}$ ) (e.g. [Royer et al. 2007](#)), which realizes the coupling between the gravity mode and inertial mode (whose restoring force is the inertial force) to establish the gravito-inertial mode inside the stars (e.g. [Mathis et al. 2014](#); [Ouazzani et al. 2017](#)). The asymptotic analysis of the gravito-inertial mode has been often performed based on the so-called traditional approximation of rotation (TAR; [Eckart 1960](#); [Lee and Saio 1997](#)), where uniform rotation is assumed and the horizontal component of the rotation angular velocity is neglected. [Bouabid et al. \(2013\)](#) have studied the  $\Delta P_g$  pattern of the fast-rotating stars based on TAR, finding that the  $\Delta P_g$  pattern is quasi-linearly related to the g-mode period and that the gradient of the general trend in the  $\Delta P_g$  pattern (as a function of the g-mode period) is determined by the rotation rate. The property has enabled us to infer the internal rotation rates of the g-mode cavity of the fast-rotating stars ([Li et al. 2019, 2020](#); [Pedersen 2022b](#)).

Another mechanism has been suggested by [Ouazzani et al. \(2020\)](#) that the inertial mode in the convective core can be coupled with the g mode, which can produce the dip structure in the  $\Delta P_g$  pattern of rapidly rotating stars. [Saio et al. \(2021\)](#) have analyzed the dips in the  $\Delta P_g$  patterns of 16  $\gamma$  Dor stars observed by the Kepler probe to infer the convective-core rotation rates of the stars, concluding that most of the stars studied are rotating almost rigidly. Similar discussions can also

be found, e.g., Lee and Saio (2020) and Tokuno and Takata (2022).

As such, rotation certainly has significant effects on  $\Delta P_g$  patterns of intermediate-mass main-sequence g-mode pulsators (for more thorough review, see Reese 2022). It is still possible that the effects of rotation on the  $\Delta P_g$  pattern can be separable from those of the sharp BV frequency variation inside stars because signatures imprinted by rotation is not oscillatory with respect to the g-mode period (Bouabid et al. 2013; Saio et al. 2021). We thus might be able to, for example, analyze a component in the  $\Delta P_g$  pattern originating from rotation and that originating from the sharp BV frequency variation independently by assuming a simple linearity among the effects. Alternatively, we can generalize the newly derived semi-analytical expression for rotating stars within the traditional approximation. These should be worth investigating in our future work.

Convective overshooting is, theoretically speaking, considered as a natural consequence of uprising mass elements having inertia (e.g. Kippenhahn et al. 2013). Multiple observational studies of stellar clusters have also favored the existence of convective overshooting in early-type main-sequence stars with the convective core (e.g. Maeder & Mermilliod 1981; Meynet et al. 1993; VandenBerg & Stetson 2004; Rosenfield et al. 2017). It is however quite difficult to evaluate effects of convective overshooting on the internal structure of stars mainly because of a lack of the understanding of physics around the convective boundary, so far forcing us to rely on phenomenological schemes to describe convective overshooting (e.g. Viallet et al. 2015). An important point is that different prescriptions of convective overshooting lead to different BV frequency profiles, then resulting in different morphologies of  $\Delta P_g$  patterns. This has strongly motivated us to carry out asteroseismic modeling to determine which prescription is most favorable to reproduce the observed  $\Delta P_g$  patterns (see Pedersen 2022a, and references therein).

One of the effects of convective overshooting on the internal structure of a star is to extend the uniformly mixed region above the convective-core boundary where the convective stability is satisfied and the squared BV frequency is positive. This could lead to a jump-like structure in the BV frequency (see around the outer edge of the grey shaded area in the middle panel of Figure 14, in which convective overshooting is treated as exponential diffusive overshooting; Herwig 2000). It is therefore expected that there is another oscillatory component in the  $\Delta P_g$  pattern in addition to that caused by the sharp BV frequency variation located around the outer edge of the chemical composition gradient. Such a

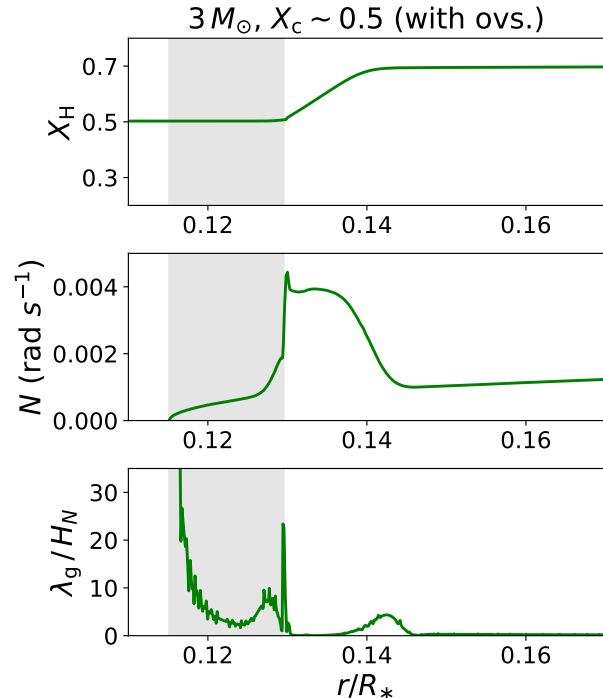


**Figure 14.** Internal properties around the convective-core boundary of the  $3 M_{\odot}$  model with  $X_c \sim 0.5$  for which convective overshooting is taken into account. Hydrogen mass content ( $X_H$ ), BV frequency ( $N$ ), and the ratio of the typical wavelength of high-order g modes to the scale height of the BV frequency ( $\lambda_g/H_N$ ) are shown from top to bottom. The horizontal axis is the fractional radius. Convective overshooting is treated as exponential diffusive overshooting (Herwig 2000) where the overshooting parameter ( $f_{ov} = 0.02$ ) is used. The overshoot zone is indicated by the grey shaded region, in which the chemical composition is uniform and the square of the BV frequency is positive.

$\Delta P_g$  pattern with double oscillatory components can be confirmed by the analytical expression of the  $\Delta P_g$  pattern derived based on the perturbative approach (see Equation A5). Note that the JWKB approximation is broken near the inner edge of the g-mode cavity where the typical wavelength of the g mode is much longer than the scale height of the BV frequency (see around the inner edge of the grey shaded area in the bottom panel of Figure 14). Accordingly,  $\Delta P_g$  patterns numerically computed with stellar models (for which convective overshooting is taken into account) exhibit rather complex behaviors compared with what the analytical expression predicts (Figure 15).

Since the location of the jump-like structure in the BV frequency is closer to the inner edge of the g-mode cavity (compared with that of the BV frequency transition caused by the chemical composition gradient), the oscillatory component in the  $\Delta P_g$  pattern related to convective overshooting should have much longer period than



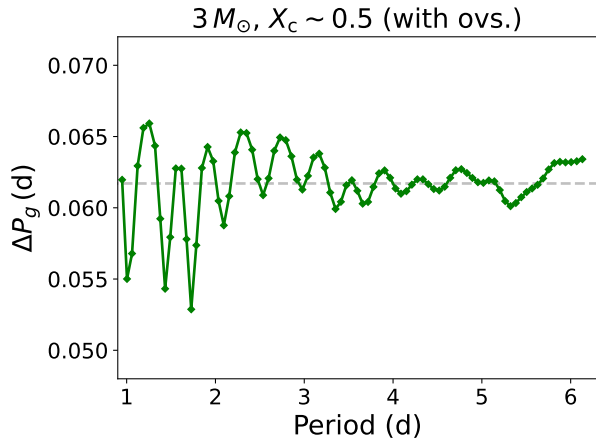


**Figure 15.**  $\Delta P_g$  pattern numerically computed based on the  $3 M_\odot$  model with  $X_c \sim 0.5$  for which convective overshooting is taken into account (the same model as that shown in Figure 14). The horizontal axis shows the g-mode period. The mean value of the  $\Delta P_g$  pattern is indicated by the grey dashed line.

that of the oscillatory component related to the outer edge of the chemical composition gradient (see Equation A5). This implies the possibility that we can study these effects independently in a similar way as we discussed effects of rotation. However, one difficulty is that it should be often the case that the number of detected modes is not enough to observe the whole structure of a long-period component in the  $\Delta P_g$  pattern. In addition, the dip structure caused by the fast rotation may complicate the situation (see discussions in Appendix A of Saio et al. 2021). Further analyses would be thus expected for comprehensive analysis of the observed  $\Delta P_g$  patterns.

## 6. CONCLUSION

1-dimensional stellar models of intermediate-mass stars ( $1.6 M_\odot < M < 6 M_\odot$ ) show that not only the size of the convective core but also the BV frequency profile around the deep radiative region just above the convective core depends strongly on the balance between the pp-chain reaction and CNO cycle. In particular, as the mass of the star becomes smaller, the pp-chain reaction becomes dominant over the CNO cycle more in the core region. For the less massive stars, the region where the pp-chain reaction is at work extends beyond the convective-core boundary and effectively smoothens the chemical composition gradient there, leading to the smaller steepness of the BV frequency gradient that is shaped like a ramp rather than a jump.

Based on the assumption that the BV frequency of less massive stars ( $M < 4 M_\odot$ ) can be modeled with a ramp function, we apply the JWKB approximation

to derive a semi-analytical expression of the  $\Delta P_g$  pattern for high-order g modes. The formulation includes a period-dependent term that represents the degree of the sharp variation in the BV frequency sensed by g modes and enables us to reproduce a trend that the amplitude of the oscillatory component in the  $\Delta P_g$  pattern decreases for longer g-mode periods. The semi-analytical expression has been validated by comparing it with  $\Delta P_g$  patterns numerically computed based on simple BV frequency models.

Tests with 1-dimensional stellar models show that the semi-analytical expression can be used for inferring the degree of the structural variation ( $B_\star$ ) in the BV frequency, achieving accuracy around  $\sim 10\%$  given that the BV frequency transition in the deep radiative region is sharp enough to validate neglecting the period dependence of the strength of the discontinuity (in the first derivative of the local wavenumber)  $A'_\star$ . For instance, the condition mentioned above is satisfied in the case of ordinary 1-dimensional stellar models with the mass larger than  $3 M_\odot$ . Thus, we might apply the fitting procedure with the semi-analytical expression presented in this study to SPB or  $\beta$  Cep stars. Parameter estimation of  $B_\star$  with the semi-analytical expression, however, does not work well for the less massive stellar models ( $M \leq 2 M_\odot$ ), which could be resolved by taking into account the period dependence of  $A'_\star$  in the semi-analytical expression. We nevertheless would like to emphasize that the most important parameter is not the mass but the sharpness of the BV frequency transition. Some less massive stars ( $M \leq 2 M_\odot$ ) might have such a sharp BV frequency transition, as is the case for KIC 11145123, that we can possibly justify applying the semi-analytical expression to these stars.

Finally, it should be noticed that dynamics such as rotation and overshooting have significant impacts on the  $\Delta P_g$  pattern as well, and therefore, further comprehensive analyses of the  $\Delta P_g$  pattern would be desirable.

We would like to express our gratitude to the NASA and *Kepler* team for the precious data. Y. H. acknowledges T. Sekii for his insightful comments. M. Takata, O. Benomar, and M. Cunha are also thanked for their constructive advices. This work was supported by MEXT as “Program for Promoting Researches on the Supercomputer Fugaku” (Toward a unified view of the universe: from large scale structures to planets, JPMXP1020200109), JSPS Grant-in-Aid for Scientific Research (A) Grant Number JP21H04492, and JSPS Grant-in-Aid for JSPS Research Fellow Grant Number JP20J15226.

## REFERENCES

- Aerts, C., Christensen-Dalsgaard, J., & Kurtz, D. W. 2010, *Asteroseismology* (Berlin: Springer)
- Aerts, C., Mathis, S., & Rogers, T. M. 2019, *ARA&A*, 57, 35
- Bedding, T. R., Mosser, B., Huber, D., et al. 2011, *Natur*, 471, 608
- Bouabid, M.-P., Dupret, M.-A., Salmon, S., et al. 2013, *MNRAS*, 429, 2500
- Brassar, P., Fontaine, G., Wesemael, F., & Hansen, C. J. 1992, *ApJS*, 80, 369
- Buysschaert, B., Aerts, C., Bowman, D. M., et al. 2018, *A&A*, 616, A148
- Christensen-Dalsgaard, J. 2012, in *ASP Conf. Ser. 462, Progress in Solar/Stellar Physics with Helio- and Asteroseismology*, ed. H. Shibahashi, M. Takata & A. E. Lynas-Gray (San Francisco, CA: ASP), 503
- Cunha, M. S., Stello, D., Avelino, P. P., Christensen-Dalsgaard, J., & Townsend, R. H. D. 2015, *ApJ*, 805, 127
- Cunha, M. S., Avelino, P. P., Christensen-Dalsgaard, J., et al. 2019, *MNRAS*, 490, 909
- Degroote, P., Briquet, M., Auvergne, M., et al. 2010, *A&A*, 519, A38
- Degroote, P., Aerts, C., Baglin, A., et al. 2010, *Natur*, 464, 259
- Eckart, G. 1960, *Hydrodynamics of oceans and atmospheres* (Oxford: Pergamon Press)
- Garcia, S., Van Reeth, T., De Ridder, J., et al. 2022, *A&A*, 662, A82
- Garcia, S., Van Reeth, T., De Ridder, J., & Aerts, C. 2022, *A&A*, 668, A137
- Gough, D. O. 1993, *Astrophysical Fluid Dynamics*, Les Houches, Session XLVII, ed. J.-P. Zahn & J. Zinn-Justin (Amsterdam: Elsevier), 399
- Gregory, P. C. 2005, *Bayesian Logical Data Analysis for the Physical Sciences: A Comparative Approach with Mathematica Support* (Cambridge: Cambridge University Press)
- Hatta, Y., Sekii, T., Takata, M., & Kurtz, D. W. 2019, *ApJ*, 871, 135
- Hatta, Y., Sekii, T., Takata, M., & Benomar, O. 2021, *ApJ*, 923, 244
- Herwig, F. 2000, *A&A*, 360, 952
- Huber, D., Silva Aguirre, V., Matthews, J. M., et al., 2014, *ApJS*, 211, 2
- Kippenhahn, R., Weigert, A., & Weiss, A. 2012, *Stellar Structure and Evolution* (Berlin, Heidelberg: Springer)
- Koch, D. G., Borucki, W. J., Basri, G. et al. 2010, *ApJL*, 713, L79
- Kurtz, D. W., Saio, H., Takata, M. et al. 2014, *MNRAS*, 444, 102
- Lee, U. & Saio, H. 1997, *ApJ*, 491, 839
- Lee, U. & Saio, H. 2020, *MNRAS*, 497, 4117
- Li, G., Van Reeth, T., Bedding, T. R., Murphy, S. J., & Antoci, V. 2019, *MNRAS*, 487, 782
- Li, G., Van Reeth, T., Bedding, T., et al. 2020, *MNRAS*, 491, 3586
- Maeder, A. & Mermilliod, J. C. 1981, *A&A*, 93, 136
- Maeder, A. 2009, *Physics, Formation and Evolution of Rotating Stars* (Berlin: Springer)
- Mathis, S., Neiner, C., & Tran Minh, N. 2014, *A&A*, 565, A47
- Metropolis, N., Rosenbluth, A., & Rosenbluth, M. 1953, *J. Chem. Phys.*, 21, 188
- Meynet, G., Mermilliod, J. C., & Maeder, A. 1993, *A&AS*, 98, 477
- Michaud, G., Alecian, G., & Richer, J. 2015, *Atomic Diffusion in Stars* (Berlin: Springer)
- Michielsen, M., Aerts, C., & Bowman, D. M. 2021, *A&A*, 650, A175
- Miglio, A., Montalbán, J., Noels, A., & Eggenberger, P. 2008, *MNRAS*, 386, 1487
- Montgomery, M. H., Metcalfe, T. S., Winget, D. E. 2003, *MNRAS*, 344, 657
- Moravveji, E., Aerts, C., Pápics, P. I., Triana, S. A., & Vandoren, B. 2015, *A&A*, 580, A27
- Moravveji, E., Townsend, R. H. D., Aerts, C., & Mathis, S. 2016, *ApJ*, 823, 130
- Moravveji, E. 2016, *MNRAS*, 455, L67
- Morel, P. & Thevenin, F. 2002, *A&A*, 390, 611
- Ouazzani, R.-M., Salmon, S. J. A. J., Antoci, V., et al. 2017, *MNRAS*, 465, 2294
- Ouazzani, R.-M., Lignières, F., Dupret, M.-A., et al. 2020, *ApJ*, 640, 10
- Pápics, P. I., Moravveji, E., Aerts, C., et al. 2014, *A&A*, 570, A8
- Pápics, P. I., Tkachenko, A., Aerts, C., et al. 2015, *ApJ*, 803, L25
- Paxton, B., Bildsten, L., Dotter, A., et al. 2011, *ApJS*, 192, 3
- Paxton, B., Cantiello, M., Arras, P., et al. 2013, *ApJS*, 208, 4
- Paxton, B., Marchant, P., Schwab, J., et al. 2015, *ApJS*, 220, 15
- Paxton, B., Schwab, J., Bauer, E. B., et al. 2018, *ApJS*, 234, 34
- Paxton, B., Smolec, R., Schwab, J., et al. 2019, *ApJS*, 243, 10
- Pedersen, M. G., Aerts, C., Pápics, P. I., Rogers, T. M. 2018, *A&A*, 614, A128
- Pedersen, M. G. 2022, *ApJ*, 940, 49
- Pedersen, M. G. 2022, *ApJ*, 930, 94
- Reese, D. R. 2022, *FrASS*, 9, 934579
- Ricker, G. R., Winn, J. N., Vanderspek, R., et al. 2014, *SPIE*, 9143, 20
- Rosenfield, P., Girardi, L., Williams, B. F., et al. 2017, *ApJ*, 841, 69
- Royer, F., Zorec, J., & Gómez, A. E. 2007, *A&A*, 463, 671
- Saio, H., Kurtz, D. W., Takata, M., et al. 2015, *MNRAS*, 447, 3264
- Saio, H., Takata, M., Lee, U., et al. 2021, *MNRAS*, 502, 5856
- Takada-Hidai, M., Kurtz, D. W., Shibahashi, H., et al. 2017, *MNRAS*, 470, 4908
- Tassoul, M. 1980, *ApJS*, 43, 469
- Tokuno, T. & Takata, M. 2022, *MNRAS*, 514, 4140
- Townsend, R. H. D. & Teitler, A. 2013, *MNRAS*, 435, 3406
- Unno, W., Osaki, Y., Ando, H., Saio, H., & Shibahashi, H. 1989, *Nonradial Oscillations of Stars* (Tokyo: University of Tokyo Press)
- VandenBerg, D. A. & Stetson, P. B. 2004, *PASP*, 116, 997
- Van Reeth, T., Tkachenko, A., Aerts, C., et al. 2015, *ApJS*, 218, 27
- Viallet, M., Meakin, C., Prat, V., & Arnett, D. 2015, *A&A*, 580, A61
- Wu, T. & Li, L. 2019, *ApJ*, 881, 86
- Wu, T., Li, Y., Deng, Z.-M., et al. 2020, *ApJ*, 899, 38

## APPENDIX

A. ANALYTICAL EXPRESSION OF G-MODE PERIOD SPACING  
DERIVED BASED ON PERTURBATION THEORY

We here present analytical expressions of the  $\Delta P_g$  pattern derived based on the perturbative approach (see also Section 3.1), in which the oscillatory component in the  $\Delta P_g$  pattern is considered as a result of perturbed g-mode eigenfrequencies that originate from a perturbation in the BV frequency. We will show two examples of how we model the perturbation in the BV frequency ( $\delta N$  hereafter): in one case,  $\delta N$  is modeled with a ramp (Appendix A.1), and in the other case, it is modeled with a convective overshoot zone (Appendix A.2).

Before going into detail, let us present an important equation that relates the perturbation in the BV frequency ( $\delta N$ ) to the perturbed g-mode period to first order:

$$-\frac{\Pi_0^{-1}}{2} \frac{\delta P_n}{P_n} = \int \left( \frac{\delta N}{N} \right) \sin^2 \left( \frac{LP_n}{2\pi} \Pi_r^{-1} + \frac{\pi}{4} \right) d\Pi_r^{-1}, \quad (\text{A1})$$

where  $P_n$  and  $\delta P_n$  represent the period of a g mode with the radial order  $n$  and the perturbed period of the g mode, respectively. The meanings of the other parameters can be found in the main text. This equation can be derived based on the variational principle (see, e.g., Montgomery et al. 2003; Miglio et al. 2008; Wu et al. 2020, for more information on the derivation).

By parameterizing the perturbation in the BV frequency  $\delta N$  so that we can analytically compute the integration in Equation (A1), we can then derive explicit expressions of the  $\Delta P_g$  pattern as a function of the g-mode periods as we will see in Appendices A.1 and A.2.

A.1. The case of  $\delta N$  parameterized with a ramp function

The parameterization of  $\delta N$  is done with a ramp function as below:

$$\frac{\delta N}{N} = \frac{1 - \alpha^2}{\alpha^2} \frac{\Pi_\star^{-1} - \Pi_r^{-1}}{\Pi_\star^{-1}} H(\Pi_\star^{-1} - \Pi_r^{-1}), \quad (\text{A2})$$

where  $H(\Pi_\star^{-1} - \Pi_r^{-1})$  represents a step function in terms of the buoyancy radius  $\Pi_r^{-1}$ . We follow the notation of Miglio et al. (2008) to express the strength of the perturbation with the term  $(1 - \alpha^2)/\alpha^2$ . Note that the buoyancy radius of the inner edge of the g-mode cavity ( $r = r_0$ ) is zero. An example of  $\delta N$  parameterized in this way is shown in Figure 8 in the main text where  $\alpha^2 = 0.99$ .

We can analytically compute the integral (A1) by inserting Equation (A2) and integrating by parts once. The result is

$$\frac{\delta P_n}{P_n} = \left( -\frac{1 - \alpha^2}{\alpha^2} \Pi_0 \Pi_\star \right) \left[ \frac{1}{2} (\Pi_\star^{-1})^2 + \frac{\omega_n}{2L} \Pi_\star^{-1} - \left( \frac{\omega_n}{2L} \right)^2 \sin \left( 2n\pi \Pi_0 \Pi_\star^{-1} \right) \right], \quad (\text{A3})$$

in which  $\omega_n = 2\pi/P_n$ . When we focus on the sinusoidal component in the expression, it is readily seen that the amplitude of the oscillatory  $\Delta P_g$  pattern is proportional to the strength of the perturbation  $(1 - \alpha^2)/\alpha^2$  and that the period of the oscillatory component is determined by a ratio between  $\Pi_0^{-1}$  and  $\Pi_\mu^{-1}$ . In addition, we see that the amplitude depends on the g-mode periods  $P_n$ . These properties are consistent with what have been pointed out by, e.g., Miglio et al. (2008).

A.2. The case of  $\delta N$  parameterized with an overshoot zone

In Appendix A.1, it is assumed that  $\delta N$  is non-zero near the inner edge of the g-mode cavity where  $\Pi_r^{-1} \sim 0$ . But it is ordinarily seen based on 1-dimensional stellar evolutionary calculations (see discussions in Section 5 of the main text) that the BV frequency is rather smooth around regions just above the convective core. This is due to the presence of the overshoot zone, in which the chemical compositions are well-mixed despite the convective stability there (the adiabatic temperature gradient  $\nabla_{\text{ad}}$  is larger than the radiative temperature gradient  $\nabla_{\text{rad}}$ ). As a result, we can assume  $\delta N \sim 0$  in the overshoot zone.

Then, the parameterization of  $\delta N$  with an overshoot zone is given as below:

$$\frac{\delta N}{N} = \begin{cases} 0 & (0 \leq \Pi_r^{-1} \leq \Pi_{\star_1}^{-1}) \\ \frac{1 - \alpha^2}{\alpha^2} \frac{\Pi_{\star_2}^{-1} - \Pi_r^{-1}}{\Pi_{\star_2}^{-1} - \Pi_{\star_1}^{-1}} H(\Pi_{\star_2}^{-1} - \Pi_r^{-1}) & (\Pi_{\star_1}^{-1} \leq \Pi_r^{-1}), \end{cases} \quad (\text{A4})$$

where  $\Pi_{\star_1}^{-1}$  and  $\Pi_{\star_2}^{-1}$  represent the buoyancy radii with which the interval  $0 \leq \Pi_r^{-1} \leq \Pi_{\star_1}^{-1}$  is the overshoot zone (where  $\delta N$  is zero) and the interval  $\Pi_{\star_1}^{-1} \leq \Pi_r^{-1} \leq \Pi_{\star_2}^{-1}$  is the sharp buoyancy ramp above the overshoot zone.

We can thus obtain the analytical expression of the  $\Delta P_g$  pattern in the case of  $\delta N$  with the overshoot zone almost in the same way as in Appendix A.1:

$$\begin{aligned} \frac{\delta P_n}{P_n} = & \left( -\frac{1-\alpha^2}{\alpha^2} \Pi_0 (\Pi_{\star_2}^{-1} - \Pi_{\star_1}^{-1})^{-1} \right) \\ & \times \left[ \frac{1}{2} (\Pi_{\star_2}^{-1} - \Pi_{\star_1}^{-1})^2 + \frac{\omega_n}{2L} (\Pi_{\star_2}^{-1} - \Pi_{\star_1}^{-1}) \cos \left( 2n\pi \Pi_0 \Pi_{\star_1}^{-1} \right) - \left( \frac{\omega_n}{2L} \right)^2 \left( \sin \left( 2n\pi \Pi_0 \Pi_{\star_2}^{-1} \right) - \sin \left( 2n\pi \Pi_0 \Pi_{\star_1}^{-1} \right) \right) \right]. \end{aligned} \quad (\text{A5})$$

We obtain the expression (A3) if we take limits  $\Pi_{\star_1}^{-1} \rightarrow 0$  and  $\Pi_{\star_2}^{-1} \rightarrow \Pi_{\star}^{-1}$ .

Equation (A5) contains two oscillatory components, one of which has a period determined by a ratio between  $\Pi_0^{-1}$  and  $\Pi_{\star_1}^{-1}$ , and the other has a period determined by a ratio between  $\Pi_0^{-1}$  and  $\Pi_{\star_2}^{-1}$ , indicating that not only a sharp feature in the BV frequency but also the extent of convective overshooting have impacts on the  $\Delta P_g$  patterns.